Cite this as:
Alena Folger, Petra Ebbinghaus, Andreas Erbe, Christina Scheu: The role of vacancy condensation for the formation of voids in TiO_2 rutile nanowires. *ACS Applied Materials & Interfaces*, **9**, 13471–13479 (**2017**). DOI: 10.1021/acsami.7b01160

Final copy-edited version of the manuscript is available from:
https://doi.org/10.1021/acsami.7b01160

The role of vacancy condensation for the formation of voids in rutile TiO_2 nanowires

Alena Folger,[†] *Petra Ebbinghaus,*[†] *Andreas Erbe,*[†‡] *Christina Scheu*[†¶]

[†]Max-Planck-Institut für Eisenforschung GmbH, Max-Planck-Str. 1, D-40237 Düsseldorf, Germany

[‡]Department of Materials Science and Engineering, NTNU, Norwegian University of Science and Technology, 7491 Trondheim, Norway

[¶]Materials Analytics, RWTH Aachen University, Kopernikusstr. 10, 52074 Aachen, Germany

ABSTRACT: Titanium dioxide nanowire arrays are incorporated in many devices for energy conversion, energy storage and catalysis. A common approach to fabricate these nanowires is based on hydrothermal synthesis strategies. A drawback of this low-temperature method is that the nanowires have a high density of defects, such as stacking faults, dislocations and oxygen vacancies. These defects compromise the performance of devices. Here we report a post-growth thermal annealing procedure to remove these lattice defects and propose a mechanism to explain the underlying changes in the structure of the nanowires. A detailed transmission electron microscopy study including in-situ observation at elevated temperatures reveals a two stage process. Additional spectroscopic analysis as well as X-ray diffraction experiments clarify the underlying mechanisms. In an early, low temperature stage, the as-grown mesocrystalline nanowire converts to a single crystal by a dehydration of surface bound OH groups. At temperatures above 500 °C a condensation of oxygen vacancies takes place, which leads to

nanowires with internal voids. These voids are faceted and covered with Ti^{3+} rich amorphous TiO_x.

Keywords: TiO_2, nanowire, vacancy condensation, transmission electron microscopy, void,

Introduction

Titanium dioxide (TiO_2) is one of the most versatile metal oxides and has been suggested for many different applications, e.g., in the fields of photocatalytic pollutant degradation, photo catalysis, solar cells, energy storage and conversion, novel biomaterials and so on.[1] Large effort is put into the development of high performing TiO_2 materials with high surface areas and low recombination rates. Especially nanostructures and hollow materials have attracted considerable attention. Within the last years many different TiO_2 nanostructures, such as meso-porous layers[2-4], cubes[5-6], tubes[7-8] or wires[9-10] were synthesized and investigated. Among these, one-dimensional nanostructures are noteworthy due to their superior properties, e.g. a large surface area and directed electron path.[11-12] Since Feng et al.[13] developed a simple solvothermal fabrication route of rutile nanowire (NW) arrays on conducting glass, these nanostructures were intensively studied. However, devices incorporating these hydrothermally grown TiO_2 NW arrays fall short of expectations, which were predicted for highly crystalline 1D materials.[14-15] One reason for the low efficiency of e.g. hybrid solar cells is the high recombination rate of charge carriers due to intrinsic point defects (e.g. oxygen vacancies, Ti interstitials) and lattice defects (e.g. edge dislocation, stacking faults). There are several strategies to overcome these limitations, like doping or limiting the diffusion of carriers in one direction e.g. by incorporation of voids into these nanostructures.[15-17] First studies on voids in rutile TiO_2 nanoparticles were performed by Turner et al.[18] and showed that these voids are facetted.[19] Since then many strategies were developed to introduce voids into TiO_2 nanostructures and various hollow TiO_2 nanostructures were synthesized and analyzed. Several microwave-assisted synthesis strategies

were developed to obtain hollow anatase TiO_2 nanocrystals, which show much higher photocatalytic activity compared to the dense counterpart.[16-17] Another approach is the calcination of precipitated precursor particles or mesocrystals, which leads to foam-like single crystals.[20-21] Although most of the hollow nanostructures investigated so far are nanoparticles, there are several reports about highly efficient devices incorporating NWs with internal voids. Apart from these reports, where the voids inside the NWs are an uncurious side effect, there are targeted methods for incorporating those voids intentionally. Wisnet et al. used a combination of $TiCl_4$ treatment and annealing of NW arrays to reduce the recombination in hybrid solar cells.[14] Recently, Liu et al. proposed a combination of helium ion implantation and subsequent annealing to introduce voids inside rutile TiO_2 NWs and thereby they enhanced the photo-electrochemical water splitting.[15] Another approach is the thermal treatment of $H_2Ti_3O_7$ NWs, which results in voids inside TiO_2 NWs.[22] However, the resulting NWs are not rutile, but possess the anatase crystal structure and the voids arise during phase transformation due to volume differences.

Although TiO_2 NW arrays with voids have been incorporated in many well-performing devices, such as solar-cells, photo electrodes and others,[14-15, 23-25] so far, no detailed study on the formation mechanism of these voids is reported. In the present study, we first demonstrate, how internal voids can be introduced into hydrothermally grown TiO_2 NW by a thermal annealing process and propose a possible mechanism, which explains the formation of the internal voids and the related property changes of the NWs.

Experimental methods

Synthesis procedure

TiO_2 nanowire were synthesized following a hydrothermal procedure described by Liu et al.[26] All chemicals were used as supplied without further purification. Typically, 150-250 µL

titanium butoxide (Ti(*n*OBu)$_4$, Sigma-Aldrich) was dropped into a mixture of 5 mL deionized water and 5 mL concentrated hydrochloric acid (37 wt%, analytical grade, Sigma-Aldrich) under vigorous stirring. Fluorine-doped tin oxide (FTO) substrates were cleaned in ultrasonic bath using isopropanol, acetone and ethanol and placed vertically in a Teflon liner. The liquid was transferred to the Teflon liner, which was placed into a steel autoclave. The hydrothermal reaction was performed at 150 °C for 3-6 hours. Afterwards, the autoclave was cooled down to room temperature. The FTO substrates, covered with TiO_2 nanowire arrays, were rinsed with deionized water and dried with compressed air. Heat treatment of the samples was performed at 500 °C for 4 hours on a hot plate in air.

Characterization

Scanning electron microscopy (SEM) analysis: SEM was applied for the morphological analysis of the nanowires in top-view and cross-section. A Zeiss Auriga Modular CrossBeam workstation equipped with an in-lens detector was used at 4 kV. Cross-section samples were prepared by breaking the FTO substrate covered with the NW array into two pieces. The fracture surface was used for imaging.

Transmission electron microscopy (TEM) analysis: Further characterization was performed in TEM. Scratched and cross sectional TEM samples of as-grown and annealed TiO_2 nanowires were prepared. For scratched TEM samples the TiO_2 nanowires were scraped off the FTO substrate. The resulting powder was dispersed on a copper grid with a holey carbon film. Conventional TEM cross-sections were prepared by embedding a sandwich of the TiO_2 nanowire array on FTO glass into a brass tube, cutting of slices, grinding, dimple grinding, and argon ion milling according to Strecker et al.[27]

A Philipps CM20 and a Jeol JEM-2200FS field emission gun instrument, both operated at 200 kV, were used for selected area electron diffraction (SAED), conventional bright field TEM

and high-resolution (HR) TEM. Heating experiments were performed on the Jeol JEM-2200FS in scanning TEM (STEM) mode using a DENSsolution double tilt heating holder and respective silicon nitride chips. Starting at 250 °C the sample was heated with 3.3 K/min up to 600 °C. This temperature was hold for 30 min. The tilt series used for the 3D reconstruction has been acquired also with the same TEM at 200 keV in high angle annular dark field (HAADF) STEM mode using a tilt range of ±70° with a variable tilt increment according to the scheme proposed by Saxton et al.[28] The tilt series was aligned using the TomoJ[29] add-on in ImageJ[30] and a discrete algebraic reconstruction technique step[31] was used for the reconstruction.

Cs-corrected STEM images and electron energy loss spectroscopy (EELS) data were acquired at 300 kV with a FEI Titan Themis 60-300 equipped with a high brightness field emission (XFEG™) source, a monochromator, an aberration-corrector for the probe-forming lens system, a BRUKER EDS Super X detector and a high-resolution electron energy loss spectrometer (Gatan high-resolution Quantum ERS energy filter). Low loss EELS data were acquired in monochromatic STEM mode with a dispersion of 0.01 eV per channel. The convergence semi angle was 23.8 mrad and the collection semi angle 35 mrad. To measure the band gap on a local scale, the zero-loss tail was removed by a power law fit and the band gap extracted using the linear fit method according to Park et al.[32] Core-loss EELS data were acquired in STEM mode with a dispersion of 0.1 eV per channel, a convergence semi angle of 23.8 mrad and a collection semi angle of 35 mrad. EELS data was taken using dual-channel aquisition.[33] All spectra were corrected for channel to channel gain variation and dark current.[34] The background was removed via a standard power law fit.[34]

X-ray diffraction (XRD) analysis: XRD measurements were carried out on a Seifert Type ID3003 THETA/THETA-diffractometer (GE Inspection Technologies), equipped with a Meteor OD detector, using Co-K_α radiation in glazing incidence XRD (GIXRD) (α=2°) to

reduce the FTO signal. The XRD patterns were recorded in (θ/2θ) mode with a 2θ scan range from 10° to 120°.

Ultra-violet-visible light (UV/Vis) spectroscopy: UV/Vis data were acquired with a Perkin Elmer Lambda 800 spectrometer, detecting the absorption spectra in a wavelength range of 300 to 950 nm with a step size of 1 nm. The detected UV/Vis data is used to determine the direct band gap by Tauc plots.[35]

Infrared (IR) measurements: Attenuated total reflection (ATR) fourier-transform IR measurements were performed in air with a Bruker VERTEX 70v spectrometer equipped with a Bruker HYPERION 3000 microscope with a 20x ATR objective. During the IR analysis the NW array is contacted by the tip of a germanium crystal (100 μm in diameter). For spectra acquisition 256 scans were averaged at a spectral resolution of 2 cm^{-1} in ambient atmosphere.

Results

The crystal structure of the as-grown and annealed TiO_2 NW arrays on FTO substrate is investigated by GIXRD (Figure 1a). All peaks either correspond to the FTO substrate (marked with a filled circle) or to rutile TiO_2 for both, the as-grown and the annealed TiO_2 NW arrays. The full-widths at half-maximum (FWHM) of the {101} and {111} peaks decrease and the peaks are shifted to higher 2 θ values for the annealed TiO_2 NWs (Figure 1b,c). The peaks were used to calculate the lattice parameters *a* and *c*. The change in peak position, FWHM, lattice parameter *a* and *c* and the axial ratio *c*/*a* are summarized in Table 1. The as-grown NWs have slightly larger lattice parameters, than the annealed NWs. Only the FWHM is considerably reduced.

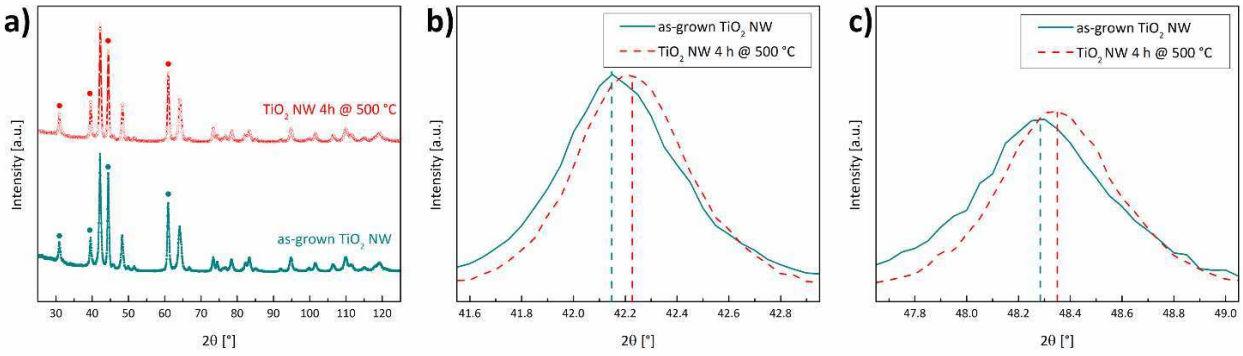

Figure 1. a) XRD pattern of as-grown and annealed TiO2 NW arrays on FTO substrate. The peaks marked with a filled dot arise from the FTO substrate. Zoom in of b) {101} and c) {111} reflection of rutile TiO_2.

sample	peak position 2θ [°]		lattice parameter [Å]		axial ratio *c*/*a*	FWHM [°]	
	{101}	**{111}**	***a***	***c***		**{101}**	**{111}**
as-grown TiO_2 NW	42.18	48.29	4.597	2.956	0.6429	0.6138	0.5984
TiO_2 NW 4h @ 500 °C	42.22	48.35	4.589	2.953	0.6434	0.5542	0.5307

Table 1. Details of XRD data and related lattice parameters (*a*, *c*) for rutile TiO_2. The accuracy of the experiment is ±0.05 %

The ATR-IR spectra of the as-grown and annealed TiO_2 NWs are presented in Figure 2. Both spectra show interference fringes.[36-38] Interference fringes are expected for IR-transparent layers of several µm thickness in direct contact with the ATR crystal. These fringes are neglected in the following discussion. Both samples have a strong absorption below 1000 cm^{-1}. This absorption is due to the Ti-O stretching modes.[39-40] The absorption peak in the IR-spectral region between 1000-1300 cm^{-1} arises from deformation vibrations of the Ti-O-H bonds.[41] The features below 1300 cm^{-1} are not affected by the heat treatment. In contrast, the absorption in the range of 4000-2500 cm^{-1} and around 1600 cm^{-1} change due to the heat treatment. These peaks can be attributed to the O-H stretching and bending modes of water bound by chemisorption and physisorption on the TiO_2 surface.[42-43] The stretching modes correspond to bridged O-H groups (around 3700 cm^{-1}), to terminal O-H groups (around

3670 cm^{-1}) and to hydrogen bonded terminal O-H groups (around 3420 cm^{-1}).[42] The peak at around 1670 cm^{-1} is an O-H bending mode of chemisorbed H_2O.[43] The sharp peak, which is visible for the as-grown TiO_2 NWs is removed due to the heat treatment. The residual features are above-mentioned interference fringes.

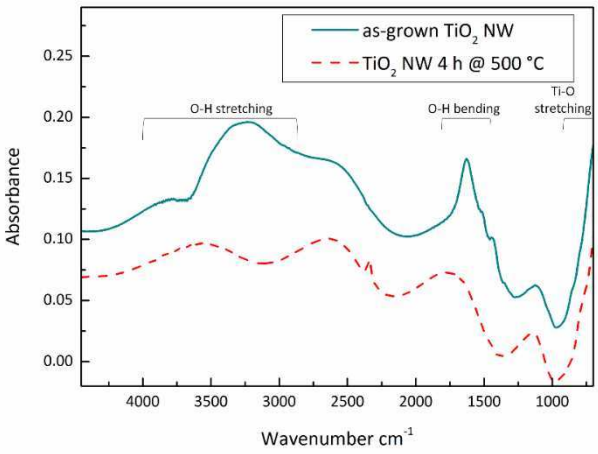

Figure 2. ATR -IR spectra of as-grown (solid line) and annealed (dashed line) TiO_2 NW arrays on FTO.

SEM investigations reveal a 1D morphology of the NW, which grow almost perpendicular to the FTO substrate (Figure 3). Neither the diameter (as-grown: 73±13 nm, annealed: 70±16 nm) nor the length (as-grown: 1005±51 nm, annealed: 1019±78 nm) of the NWs is affected by the heat treatment. However, the rough morphology at the wire top of the as-grown nanowires is smoothed during the heat-treatment.

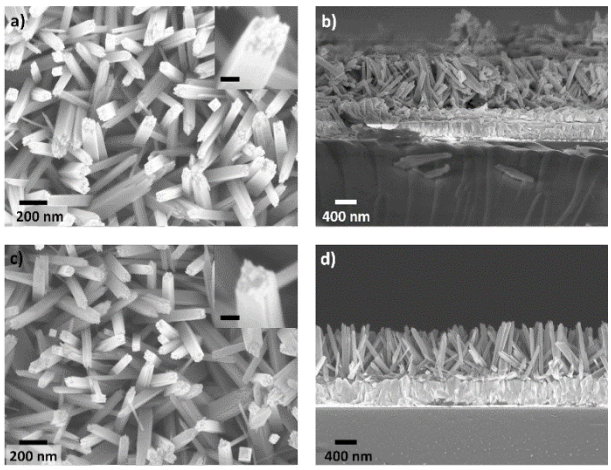

Figure 3. SEM top view (a,c) and cross-section (b,d) micrographs of as-grown (a,b) and annealed (c,d) TiO_2 NW on FTO. The insets in a) and c) show a zoom in of a single NW with changed morphology at the wire top. The scale bar of the inset images are 40 nm.

TEM images of scratched off NWs before and after annealing (see Figure 4a,e) confirm the SEM results. The as-grown TiO_2 NWs consist of a single-crystalline shell and a core with a high defect density building up a V-shaped defect cascade towards the wire top, as observed in earlier studies.[44] An edge dislocation is representatively shown in Figure 4c. Additionally, the NW splits into thin nanofibers (diameter: 6.1 nm), which results in a rough morphology at the wire top. The dark signal in the HAADF STEM image (see Figure 4d) parallel to the growth direction of the NW indicates a lower density or open space between the fibers. We identified it as internal surfaces between the nanofibers, which lead to a large internal free surface area of the as-grown NWs. The overall surface area-to-volume-ratio for a NW with 6.1 nm thick fibers is 0.66 nm^2/nm^3 with the {110} facets (surface energy per unit area (E_{110}) is 0.42 J/m^2 [45]) representing the main surface planes. By neglecting the surface at the top end of the fibers (mainly {111} and {001} facets) one can calculate the surface energy density of the as-grown NWs to $E_{surface,ag}=2.8*10^8$ J/m^3. However, the internal surfaces are not accessible for any processes related to photo catalysis or solar cells, as the spacing between the nanofibers (0.50±0.16 nm) is too small for water or dye molecules to diffuse inside. The corresponding

SAED pattern of the as-grown TiO_2 nanowire (see Figure 4b) shows a highly oriented rutile TiO_2 crystal structure, differentiating from a SAED pattern of a single-crystal in [110] zone axis only by the streaking of the diffraction spots along the [110] direction. Thus the nanofibers are highly oriented with a [001] growth direction.

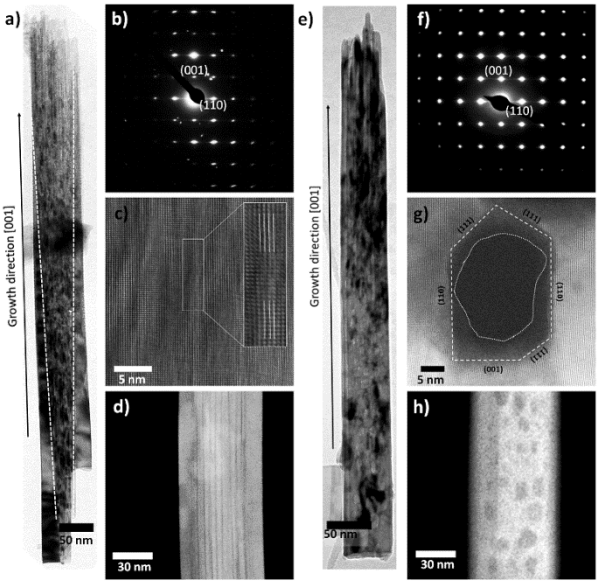

Figure 4. TEM micrographs of an as-grown (a-d) and an annealed (e-h) NW. BF TEM images (a,e) and corresponding SAED pattern (b,f) indicate a rutile crystal modification for both NWs. The HR TEM image shows an edge dislocation for the as-grown NW (c). HR HAADF STEM image of a faceted void for annealed NW (g). HAADF STEM images indicate that the as-grown NW is built by a bundle of nanofibers (d) and the annealed NW comprises voids (h). Both images are taken from representative areas located in the center of the NW.

For NWs heated at 500°C for 4 h no lattice defects are detectable, and the fibers are gown together, as there is no dark signal in the HAADF STEM image parallel to the growth direction (see Figure 4h). Only at the NW top some fiber like morphology is visible. These residuals of the nanofibers are also grown together resulting in thicker nanofibers (diameter: 8.8 nm) and a much smoother morphology at the wire top. The merging of the nanofibers is a slow process, which starts already at comparable low temperatures of around 250 °C (see Movie 1). The

corresponding SAED pattern of the annealed TiO_2 nanowire (Figure 4f) resembles a single-crystalline rutile TiO_2 crystal structure without any streaking, as both the lattice defects and the nanofibers are removed during the heat treatment. Instead of the defect-rich nanofiber bundles, the HAADF STEM image shows dark appearing features with elongated bipyramidal shape. According to TEM tomography reconstructions, these features can be attributed to voids inside the NW (see Movie 2). Using in-situ TEM heating experiments (see Movie 1) we could show that within one NW, all voids form almost simultaneously as soon as a critical temperature (around 500 °C) is reached. The voids are immediately formed in their final shape and show no change in shape or size during further annealing at 600 °C for 30 min. Due to the voids, annealed NWs also exhibit an internal free surface area. The surface area-to-volume ratio for an annealed nanowire (originating from a NW with 6.1 nm thick nanofibers in the as-grown state) is 0.1316 nm^2/nm^3. HR STEM images prove that these voids are close to the inverse Wulff's shape of rutile TiO_2 with main contributions of the {001} (E_{110}≈1.15 J/m^2)[45], {110} (E_{110}≈0.42 J/m^2),[45] and {111}(E_{110}≈1.33 J/m^2)[45] planes. For Wulff's shape like voids the average surface energy per unit surface thus can be calculated to E_{Wulff}≈0.75 J/m^2 resulting in a surface energy density of $E_{surface,HT}=9.9*10^7$ J/m^3 for annealed NWs. However, as these voids are internal voids, these surfaces are not accessible for any chemical reactions. Cross-section TEM samples allow an analysis of the structure of these voids in more detail. Figure 4g shows that the crystalline area adjacent to the void is not distorted, and that the voids are not entirely hollow, but the void surface is covered with an amorphous titanium oxide phase.

To probe the electronic structure of the NWs, we performed an EELS analysis of as-grown and annealed TiO_2 NWs. The energy-loss near-edge fine structure (ELNES) of the Ti-$L_{2,3}$ edge and the O-K edge are shown in Figure 5. Both spectra are recorded over a large area, representing the averaged bonding behavior and oxidation state of the atomic species of each type of nanowire. The Ti-$L_{2,3}$ edge consists mainly of two doublets, representing the t_{2g} and e_g peaks

of the Ti-L_3 edge at lower energy losses and the Ti-L_2 edge at higher energy losses, respectively. The edge onset (457.5 eV) and the peaks are not shifted with respect to each other and are close to literature values for bulk rutile TiO_2.[46-47] The $I(L_2)/I(L_3)$ intensity ratio is calculated as changes in this ratio are related to the Ti valance state. The analysis was done according to the procedure described by Stoyanov et al. using the following equation:[48]

$$\frac{Ti^{4+}}{\sum Ti} = \left(ln\left(\frac{\frac{I(L_2)}{I(L_3)} - 0.87953}{0.21992} \right) \right) \cdot 0.21767$$

For both, the $Ti^{4+}/\sum Ti$ (with $\sum Ti = Ti^{4+} + Ti^{3+}$) is around 80 %. Thus the averaged electronic structure of the NW does not change during heat treatment and no oxidation of incorporated Ti^{3+} to Ti^{4+} takes place within the detection limit. This result is emphasized by the O-K edge, which does neither change in shape nor in intensity, indicating that the heat treatment in air does not result in any oxygen uptake into the NW. Although the average electronic structure of the heat-treated NWs does not differ from the one of the as-grown NWs, one can detect local changes in the electronic structure. Figure 6 shows an EELS map and the corresponding EEL spectra of an annealed NW, which was thinned for TEM observation until the top and bottom surface of the void was removed. This enables the analysis of the amorphous material covering the void surface, without contributions of the crystalline rutile TiO_2, which surrounds the void. The EELS map is color-coded according to the onset of the Ti-$L_{2,3}$ edge where red represents an edge onset below and blue an edge onset above 457 eV, respectively. The Ti-$L_{2,3}$ edge of the amorphous TiO_x material covering the void surface is shifted by 1 eV to lower energies. The amount of Ti^{4+} is calculated by the $I(L_2)/I(L_3)$ intensity ratio and is around 70 % for the rutile TiO_2, in which the void is embedded and around 35 % for the amorphous part at the void surface. Figure 6d shows the variation of Ti^{4+} concentration in the area of such a void. Both,

the shift of the edge onset and the lower amount of Ti^{4+} indicate that amorphous material at the void surface consists of reduced TiO_{2-x}.

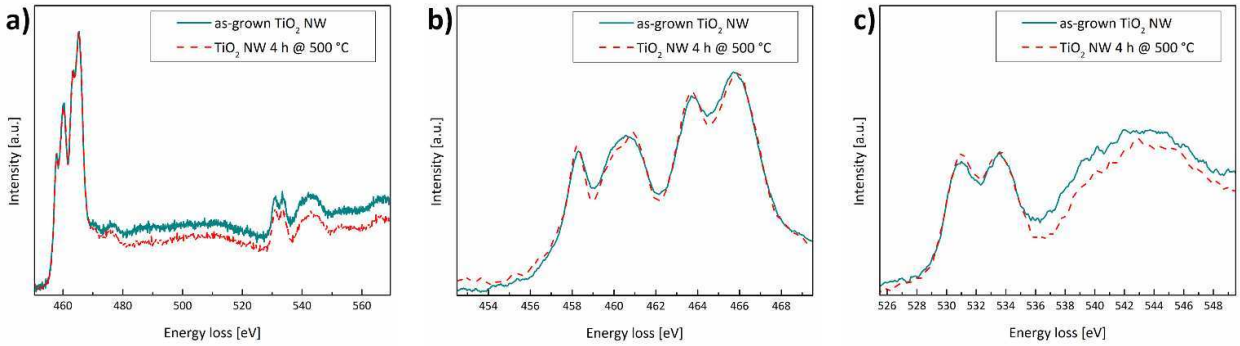

Figure 5. a) Core-loss EELS spectra of an as-grown and an annealed TiO_2 NW showing the Ti-$L_{2,3}$ and O-K edge. b) Ti-$L_{2,3}$ ELNES with t_{2g} e_g splitting caused by the distorted oxygen octahedral surrounding Ti atoms and c) O-K ELNES.

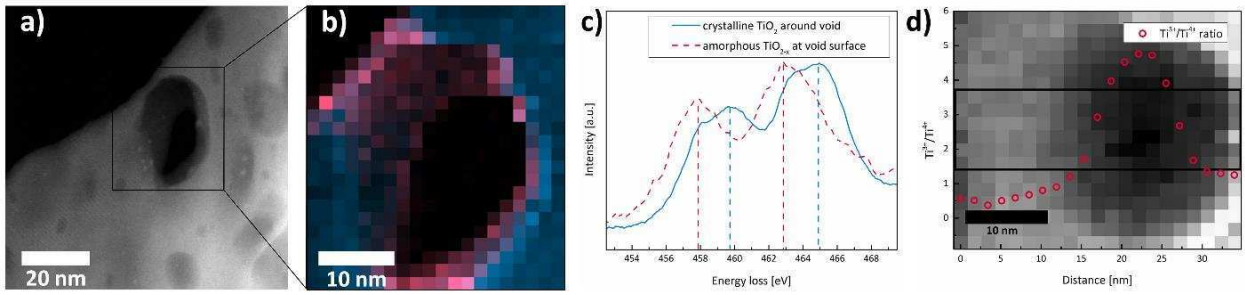

Figure 6. a) HAADF-STEM image of an annealed TiO_2 NW after Ar^+ ion milling with the area marked, which was used for STEM-EELS measurements. Please note that the amorphous layer in the right part is viewed edge on, while the part in the left is inclined and appears much more extended due to projection. b) The corresponding EELS map is color-coded according to the edge onset of the Ti-$L_{2,3}$ edge (red: edge onset below 457 eV, blue: edge-onset above 457 eV). c) Corresponding EEL spectra for the crystalline (solid line) and amorphous (dashed line) area. d) shows the Ti^{3+}/Ti^{4+} ratio in the area of a void.

To investigate the influence of the changes in crystal and electronic structure with respect to the optical properties, the band gap of the as-grown and annealed TiO_2 NWs was investigated.

The band gap averaged over an entire NW array is determined by UV/Vis data based Tauc plots for an direct semiconductor (see Figure 7a). This Tauc plot shows an optical band gap of 2.88±0.09 eV for the as-grown NWs and a band gap of 2.56±0.03 eV for the annealed NW array. Although the measurements show that both materials weakly absorb blue light, the NW arrays appear white, which might be related to a strong light reflection caused by the NW array. The signal at energies below the optical band gap arise from tails of the valence and conduction band. The width of this Urbach tail, the Urbach energy, is 0.62±0.01 eV for the as-grown NWs and 0.49±0.01 eV for the annealed NWs. In addition, the band gap of a single NW for each, the as-grown and the annealed state, is determined by EELS measurements in the TEM. The corresponding, zero-loss subtracted, low-loss EEL spectra for the as-grown and the annealed NW are shown in Figure 7b. These measurements show a reduction of the optical band gap by the heat treatment from 2.8±0.1 eV to 2.4±0.1 eV. Results from EELS and the Tauc plot agree within double standard deviation.

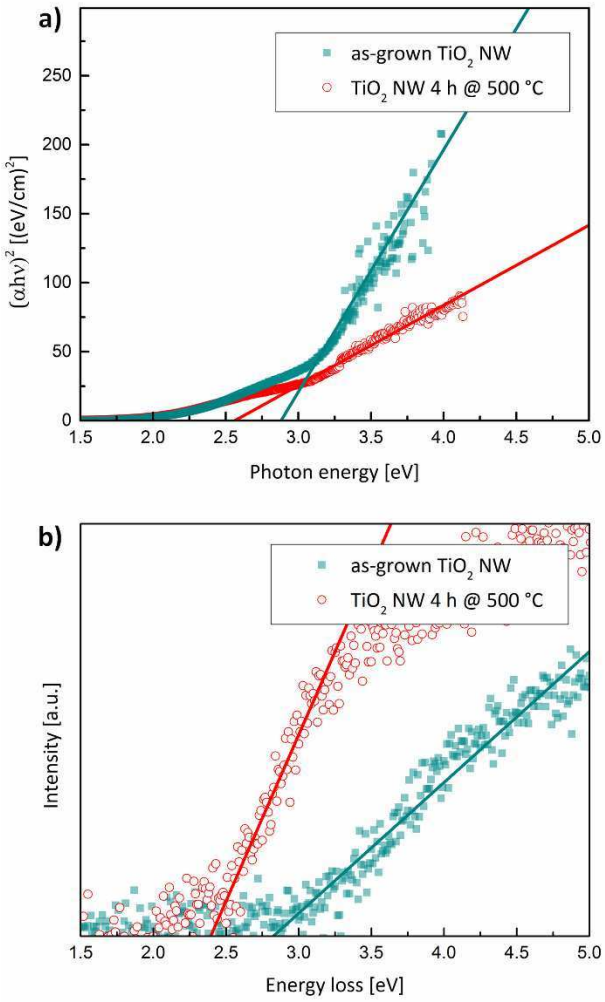

Figure 7. Optoelectronic properties of the as-grown (filled squares) and annealed (open circles) NWs. a) UV/Vis based Tauc plots of NW arrays and b) low-loss EEL spectra of single NWs after removing the zero-loss peak.

Discussion

In the following, we present a detailed description of the as-grown and annealed NWs, using the obtained morphological, crystallographic and spectroscopic results, and propose a possible mechanism to explain the formation of the voids.

HR STEM, electron diffraction and XRD reveal that the as-grown NWs consist of single-crystalline like rutile TiO_2 nanofibers, which bundle. The nanofibers grow along the [001] direction and are highly oriented with respect to each other, resulting in a mesocrystalline

material. These findings are in good agreement with previous studies on hydrothermally grown NWs.[44, 49-50] According to our IR measurements, we have a high amount of hydrogen bonded OH groups on the surfaces of these NWs. Jordan et al. found that such hydrogen bonded OH groups are present on the surface of the thin fibers and hydrogen bonds are formed between two of these fibers.[50] The distribution of distances between nanofibers and the consequent differences in hydrogen bond length may contribute to the broadening of the IR absorption peaks. The broadened peaks in the XRD and the streaking of the electron diffraction spots originate not only from the thin fibers, but also from the lattice defects inside the NW. The main defects detected in HR TEM are edge dislocations, as shown before.[44] The amount of dislocations is difficult to determine, but the narrowing of the X-ray diffraction peaks by around 10 % during annealing and the strong contrast of the V-shaped dislocation cascade (Figure 4 a) indicate that the overall concentration of dislocations must be quiet high in the as-grown NW. In addition, the spectroscopic analysis revealed a high Ti^{3+} concentration of about 20 % within the entire NW, however both, XRD and electron diffraction experiments prove the rutile crystal structure and exclude the existence of any Magneli phases such as Ti_4O_7, Ti_6O_{11} or Ti_7O_{13}.[51-52] Instead, the shift of the Ti $L_{2,3}$-edge of Ti is caused by an incorporation of oxygen vacancies (O_{vac}) in the crystal structure, leading to the expanded rutile TiO_2 unit cell of the as-grown NWs compared to bulk TiO_2.[53] As the axial ratio is the same as reported for bulk rutile TiO_2 there is no evidence for ordering of the O_{vac} along special lattice planes.

After the heat treatment, the NW morphology and the rutile crystal structure are preserved, thus we can exclude any phase transformation taking place during the heat treatment. This result is in good agreement with previous studies, which showed that rutile TiO_2 is the thermodynamically most stable TiO_2 phase.[54] Consequently, oxygen deficiency does not influence the thermodynamics of rutile TiO_2. Although the NW morphology in general does not change, there is a significant change in the internal structure. The hydrogen bridged O-H

groups, which are at the surface of the fibers in the as-grown NWs are removed, as the IR absorption peak around 3400 cm^{-1} disappears. The physisorbed water evaporates as well. The nanofiber bundle transforms into a single crystal incorporating voids. These voids are anti-crystals with the Wulff's shape of rutile TiO_2 and intercalate perfectly in the lattice without causing significant stresses in the crystal structure. From a rough estimation, the volume fraction of the voids with respect to the entire NW volume is around 25 %, which results from the rearrangement of the free space between the nanofibers (13 %) and the volume covered by O_{vac} (5-11%). The calculated volume fractions are in good accordance, but it is noteworthy that the errors are high, especially because the charge of the O_{vac} is unknown and thus deriving the number of O_{vac} (10-20 % of O in TiO_2) from the amount of Ti^{3+} is prone to error. Similar voids are also formed in rutile TiO_2 nanoparticles.[18-19] Along with the nanofibers, also the lattice defects are removed and thus the XRD shows sharper peaks and the streaking of the electron diffraction peaks is not present anymore. Although the NWs are heated in air, there is no change in the Ti $L_{2,3}$ edge averaged over an entire NW. Thus on a global scale, no oxidation takes place. The stability against oxidation might be related to the perfect single-crystalline surface of the NW even in the as-grown state, which inhibits the penetration of oxygen atoms. Consequently, the oxygen content in the atmosphere is no decisive factor for the processes taking place inside the NW upon annealing. However, locally the electronic structure of the NW does change significantly due to the heat treatment. HR STEM images show that there is no sharp rutile-vacuum interface for the voids, but the voids are covered with an amorphous TiO_x phase. According to the EELS data, this phase has a significantly higher amount of Ti^{3+}, which is up to 80% of Ti^{3+} in the amorphous material. However, one has to take into account that these samples are Ar^+ ion milled. Ar^+ ion milling can produce oxygen deficient samples due to the different sputter rates of Ti and O.[55-56] The Ti^{3+} concentration of these samples is slightly overestimated due to Ar^+ sputtering. As this effect is homogeneous over the entire TEM sample, the concentration variations are not an artifact and we can state that a vacancy condensation

takes place. Coincident with the accumulation of the Ti^{3+} at the inner void surface the unit cell is contracted, compared to the as-grown state, indicating a lower oxygen vacancy concentration in the rutile lattice.[53]

All these findings lead to the following 2 step mechanism, which explains the transformation taking place inside a hydrothermally grown rutile TiO_2 NW upon annealing. We postulate a 2 step mechanism as there are two different phenomena: The mesocrystal merging to a single crystal and the condensation of the O_{vac} to form the voids.

In a first step, a condensation reaction at the hydrogen bonded OH-groups takes place. The dehydratisation is accompanied by the formation of a new Ti-O-Ti bond, which connects two thin nanofibers. These fibers are only present in the as-grown state. It starts at the beginning of the fiber splitting close to the center part of the NW, as the distance between two fibers is closest there. This process is repeated multiple times and thus the nanofibers merge together in a zipper-like condensation process. This condensation starts already at quiet low temperatures of around 250 °C and is a rather slow process (see Movie 1). The produced water molecules leave the NW as they are gaseous at the annealing temperature. As all the Ti-O-H bonds are replaced by Ti-O-Ti bonds there is neither a global nor a local change in the oxidation state of the Ti during this process and the Ti^{4+}/Ti^{3+} ratio remains the same as in the as-grown state.

In a second step, an agglomeration of O_{vac} takes place. Due to the low temperature during the hydrothermal growth there is a high concentration of defects, especially O_{vac} in the rutile crystal structure. As the nanofibers merge together, the O_{vac} can diffuse within the NW. Upon reaching a critical temperature (around 500 °C) the O_{vac} condense rapidly and the voids with inverse Wulff's shape are formed. Using in-situ TEM heating experiments (see Movie 1) we could show that within one NW, all voids form almost simultaneously. The voids are immediately formed in their final shape and show no change in shape or size during further annealing at

600 °C. Such a vacancy condensation is well known for metals,[57-58] however it was not observed for metal oxides so far.

Our findings show that the oxygen vacancy concentration within the rutile crystal structure is significantly decreased due to the vacancy condensation upon annealing. This finding is key to understand the change in properties. According to calculations the band gap is directly linked to the concentration of O_{vac}.[59] Thus the as-grown NWs with high O_{vac} concentration inside the rutile crystal structure exhibit a larger band gap and the annealed NWs with less O_{vac} in the rutile crystal structure have a smaller band gap. This change in band gap corresponds to the band gap energies measured by UV/Vis and low loss EELS. Concurrently, the Urbach energy is decreased after the heat treatment, which indicates a lower degree of lattice disorder and less charged impurities such as O_{vac} in the crystal structure.[60] Consequently deep trap states in the band gap must have been reduced[61-63] and the recombination rate of electron-hole pairs created during illumination for the annealed NWs should significantly decrease. Furthermore, the oxygen deficient, amorphous material at the void surface has a good hole conduction and thus some of the h^+ can be injected into the oxygen deficient amorphous material.[64] The trapped h^+ cannot recombine with free e^- and the amount of generated charges is increased.

Conclusion

We have proposed a 2 step mechanism that explains the changes taking place inside a hydrothermally grown TiO_2 NW upon annealing at 500 °C in air. Rutile TiO_2 NW arrays were synthesized on FTO glass substrates. These NWs were investigated in the as-grown state and after a 4 h heat treatment at 500 °C in air. TEM, XRD and EELS investigations revealed highly defective, mesocrystalline NWs for the as-grown state with a high amount of lattice defects (edge dislocations and O_{vac}). Upon annealing, lattice defects are removed and the mesocrystal merges to a single crystal. Concurrently, the O_{vac} condense in Wulff-shaped voids, which are

covered with amorphous TiO_x. As the defects in the rutile crystal structure are removed, the properties of the material are changed. The band-gap is narrowed, and mid-band gap states must have been reduced as a consequence of the vacancy condensation. One is thus expecting reduced carrier recombination, as the amount of O_{vac} in the rutile crystal structure is decreased significantly.

AUTHOR INFORMATION

Corresponding Author

*E-mail: scheu@mpie.de.

Author Contributions

The manuscript was written through contributions of all authors. All authors have given approval to the final version of the manuscript

Funding Sources

This work was funded by the German Research Foundation (DFG) via the project *Identification and overcoming of loss mechanisms in nanostructured hybrid solar cells - pathways to more efficient devices*.

ACKNOWLEDGMENT

The authors thank Lukas Schmidt-Mende, Julian Kalb and Martin Palm for fruitful discussions, Benjamin Breitbach for XRD measurements and Andreas Wisnet for support of the 3D reconstruction of the TEM tilt series.

SUPPORTING INFORMATION

Two movies are available.

Movie 1: In-situ heating experiment in the TEM

Movie 2: 3D reconstruction of the annealed NW

REFERENCES

1. Ge, M.; Cao, C.; Huang, J.; Li, S.; Chen, Z.; Zhang, K.-Q.; Al-Deyab, S. S.; Lai, Y., A Review of One-Dimensional TiO_2 Nanostructured Materials for Environmental and Energy Applications. *J. Mater. Chem. A* **2016**, *4*, 6772-6801.
2. Nedelcu, M.; Lee, J.; Crossland, E. J. W.; Warren, S. C.; Orilall, M. C.; Guldin, S.; Huttner, S.; Ducati, C.; Eder, D.; Wiesner, U.; Steiner, U.; Snaith, H. J., Block Copolymer Directed Synthesis of Mesoporous TiO_2 for Dye-Sensitized Solar Cells. *Soft Matter* **2009**, *5*, 134-139.
3. Lee, J.; Orilall, M. C.; Warren, S. C.; Kamperman, M.; DiSalvo, F. J.; Wiesner, U., Direct Access to Thermally Stable and Highly Crystalline Mesoporous Transition-Metal Oxides with Uniform Pores. *Nat. Mater.* **2008**, *7*, 222-228.
4. Szeifert, J. M.; Fattakhova-Rohlfing, D.; Georgiadou, D.; Kalousek, V.; Rathouský, J.; Kuang, D.; Wenger, S.; Zakeeruddin, S. M.; Grätzel, M.; Bein, T., "Brick and Mortar" Strategy for the Formation of Highly Crystalline Mesoporous Titania Films from Nanocrystalline Building Blocks. *Chem. Mater.* **2009**, *21*, 1260-1265.
5. Chae, J.; Kang, M., Cubic Titanium Dioxide Photoanode for Dye-Sensitized Solar Cells. *J. Power Sources* **2011**, *196*, 4143-4151.
6. Yang, X.; Yang, Y.; Hou, H.; Zhang, Y.; Fang, L.; Chen, J.; Ji, X., Size-Tunable Single-Crystalline Anatase TiO_2 Cubes as Anode Materials for Lithium Ion Batteries. *J. Phys. Chem. C* **2015**, *119*, 3923-3930.
7. Park, M.; Heo, A.; Shim, E.; Yoon, J.; Kim, H.; Joo, H., Effect of Length of Anodized TiO_2 Tubes on Photoreactivity: Photocurrent, Cr(VI) Reduction and H_2 Evolution. *J. Power Sources* **2010**, *195*, 5144-5149.
8. Macak, J. M.; Albu, S. P.; Schmuki, P., Towards Ideal Hexagonal Self-Ordering of TiO_2 Nanotubes. *Phys. Status Solidi RRL* **2007**, *1*, 181-183.
9. Huang, X.; Pan, C., Large-Scale Synthesis of Single-Crystalline Rutile TiO_2 Nanorods via a One-Step Solution Route. *J. Cryst. Growth* **2007**, *306*, 117-122.
10. Wu, W. Q.; Lei, B. X.; Rao, H. S.; Xu, Y. F.; Wang, Y. F.; Su, C. Y.; Kuang, D. B., Hydrothermal Fabrication of Hierarchically Anatase TiO_2 Nanowire Arrays on FTO Glass for Dye-Sensitized Solar Cells. *Sci. Rep.* **2013**, *3*, 1352.
11. Ohsaki, Y.; Masaki, N.; Kitamura, T.; Wada, Y.; Okamoto, T.; Sekino, T.; Niihara, K.; Yanagida, S., Dye-Sensitized TiO_2 Nanotube Solar Cells: Fabrication and Electronic Characterization. *Phys. Chem. Chem. Phys.* **2005**, *7*, 4157-4163.
12. Zhu, K.; Neale, N. R.; Miedaner, A.; Frank, A. J., Enhanced Charge-Collection Efficiencies and Light Scattering in Dye-Sensitized Solar Cells using Oriented TiO_2 Nanotubes Arrays. *Nano Lett.* **2007**, *7*, 69-74.
13. Feng, X.; Shankar, K.; Varghese, O. K.; Paulose, M.; Latempa, T. J.; Grimes, C. A., Vertically Aligned Single Crystal TiO_2 Nanowire Arrays Grown Directly on Transparent Conducting Oxide Coated Glass: Synthesis Details and Applications. *Nano Lett.* **2008**, *8*, 3781-3786.
14. Wisnet, A.; Bader, K.; Betzler, S. B.; Handloser, M.; Ehrenreich, P.; Pfadler, T.; Weickert, J.; Hartschuh, A.; Schmidt-Mende, L.; Scheu, C.; Dorman, J. A., Defeating Loss Mechanisms in 1D TiO_2-Based Hybrid Solar Cells. *Adv. Funct. Mater.* **2015**, *25*, 2601-2608.
15. Liu, Y.; Shen, S.; Ren, F.; Chen, J.; Fu, Y.; Zheng, X.; Cai, G.; Xing, Z.; Wu, H.; Jiang, C., Fabrication of Porous TiO_2 Nanorod Array Photoelectrodes with Enhanced Photoelectrochemical Water Splitting by Helium Ion Implantation. *Nanoscale* **2016**, *8*, 10642-10648.

16. Ren, L.; Li, Y.; Hou, J.; Zhao, X.; Pan, C., Preparation and Enhanced Photocatalytic Activity of TiO_2 Nanocrystals with Internal Pores. *ACS Appl. Mater. Interfaces* **2014**, *6*, 1608-1615.
17. Chen, Y.; Li, W.; Wang, J.; Gan, Y.; Liu, L.; Ju, M., Microwave-Assisted Ionic Liquid Synthesis of Ti^{3+} Self-Doped TiO_2 Hollow Nanocrystals with Enhanced Visible-Light Photoactivity. *Appl. Catal., B* **2016**, *191*, 94-105.
18. Turner, S.; Bonevich, J. E.; Maslar, J. E.; Aquino, M. I.; Zachariah, M. R., Transmission Electron Microscopy and Electron Holography of Nanophase TiO_2 Generated in a Flame Burner System. *Nanophase and Nanocomposite Materials II* **1997**, *457*, 93-98.
19. Turner, S., Characterization of Voids in Rutile Nanoparticles by Transmission Electron Microscopy. *Nanophase and Nanocomposite Materials III* **2000**, *581*, 467-472.
20. Liu, S.; Wang, W.; Chen, J.; Li, J.-G.; Li, X.; Sun, X.; Dong, Y., Foamed Single-Crystalline Anatase Nanocrystals Exhibiting Enhanced Photocatalytic Activity. *J. Mater. Chem. A* **2015**, *3*, 17837-17848.
21. Liu, Y.; Luo, Y.; Elzatahry, A. A.; Luo, W.; Che, R.; Fan, J.; Lan, K.; Al-Enizi, A. M.; Sun, Z.; Li, B.; Liu, Z.; Shen, D.; Ling, Y.; Wang, C.; Wang, J.; Gao, W.; Yao, C.; Yuan, K.; Peng, H.; Tang, Y.; Deng, Y.; Zheng, G.; Zhou, G.; Zhao, D., Mesoporous TiO_2 Mesocrystals: Remarkable Defects-Induced Crystallite-Interface Reactivity and their In Situ Conversion to Single Crystals. *ACS Cent. Sci.* **2015**, *1*, 400-408.
22. Lei, Y.; Li, J.; Chen, F.; Wang, Z.; Liu, H.; Ma, X.; Liu, Z., In Situ Observation and Investigation on the Formation Mechanism of Nanocavities in TiO_2 Nanofibers. *CrystEngComm* **2016**, *18*, 7772-7779.
23. Zhao, Y.; Gu, X.; Qiang, Y., Influence of Growth Time and Annealing on Rutile TiO_2 Single-Crystal Nanorod Arrays Synthesized by Hydrothermal Method in Dye-Sensitized Solar Cells. *Thin Solid Films* **2012**, *520*, 2814-2818.
24. Su, J.; Guo, L., High Aspect Ratio TiO_2 Nanowires Tailored in Concentrated HCl Hydrothermal Condition for Photoelectrochemical Water Splitting. *RSC Adv.* **2015**, *5*, 53012-53018.
25. Liu, Y.; Liu, C.; Li, J., Flexible Free-Standing Hydrogen-Treated Titanium Dioxide Nanowire Arrays as a High Performance Anode for Lithium Ion Batteries. *J. Mater. Chem. A* **2014**, *2*, 15746-15751.
26. Liu, B.; Aydil, E. S., Growth of Oriented Single-Crystalline Rutile TiO_2 Nanorods on Transparent Conducting Substrates for Dye-Sensitized Solar Cells. *J. Am. Chem. Soc.* **2009**, *131*, 3985-3990.
27. Strecker, A.; Salzberger, U.; Mayer, J., Specimen Preparation for Transmission Electron Microscopy (TEM) - Reliable Method for Cross Sections and Brittle Materials. *Prakt. Metallogr.* **1993**, *30*, 482-495.
28. Saxton, W. O.; Baumeister, W.; Hahn, M., Three-dimensional Reconstruction of Imperfect Two-Dimensional Crystals. *Ultramicroscopy* **1984**, *13*, 57-70.
29. Messaoudii, C.; Boudier, T.; Sanchez Sorzano, C. O.; Marco, S., TomoJ: Tomography Software for Three-Dimensional Reconstruction in Transmission Electron Microscopy. *BMC Bioinf.* **2007**, *8*, 288-296.
30. Schneider, C. A.; Rasband, W. S.; Eliceiri, K. W., NIH Image to ImageJ: 25 Years of Image Analysis. *Nat. Methods* **2012**, *9*, 671-675.
31. Zürner, A.; Doblinger, M.; Cauda, V.; Wei, R.; Bein, T., Discrete Tomography of Demanding Samples Based on a Modified SIRT Algorithm. *Ultramicroscopy* **2012**, *115*, 41-49.
32. Park, J.; Heo, S.; Chung, J.; Kim, H.; Park, G. S., Bandgap Measurement of Dielectric Thin Films by Using Monochromated STEM-EELS. *Microsc. Microanal.* **2007**, *13*, 1306-1307.
33. Scott, J.; Thomas, P. J.; Mackenzie, M.; McFadzean, S.; Wilbrink, J.; Craven, A. J.; Nicholson, W. A., Near-Simultaneous Dual Energy Range EELS Spectrum Imaging. *Ultramicroscopy* **2008**, *108*, 1586-1594.
34. Egerton, R. F., Electron Energy-Loss Spectroscopy in the TEM. *Rep. Prog. Phys.* **2009**, *72*, 16502-16525.
35. Tauc, J.; Grigorovici, R.; Vancu, A., Optical Properties and Electronic Structure of Amorphous Germanium. *Phys. Status Solidi B* **1966**, *15*, 627-637.
36. Yamamoto, K.; Ishida, H., Optical Theory Applied to Infrared Spectroscopy. *Vib. Spectrosc.* **1994**, *8*, 1-36.
37. Reithmeier, M.; Erbe, A., Application of Thin-Film Interference Coatings in Infrared Reflection Spectroscopy of Organic Samples in Contact with Thin Metal Films. *Appl. Opt.* **2011**, *50*, 301-308.

38. Reithmeier, M.; Erbe, A., Dielectric Interlayers for Increasing the Transparency of Metal Films for Mid-Infrared Attenuated Total Reflection Spectroscopy. *Phys. Chem. Chem. Phys.* **2010**, *12*, 14798-14803.
39. Qu, Z. W.; Kroes, G. J., Theoretical Study of the Electronic Structure and Stability of Titanium Dioxide Clusters $(TiO_2)_n$ with n = 1-9. *J. Phys. Chem. B* **2006**, *110*, 8998-9007.
40. Kakuma, Y.; Nosaka, A. Y.; Nosaka, Y., Difference in TiO_2 Photocatalytic Mechanism Between Rutile and Anatase Studied by the Detection of Active Oxygen and Surface Species in Water. *Phys. Chem. Chem. Phys.* **2015**, *17*, 18691-18698.
41. Bezrodna, T.; Puchkovska, G.; Shymanovska, V.; Baran, J.; Ratajczak, H., IR-Analysis of H-Bonded H_2O on the Pure TiO_2 Surface. *J. Mol. Struct.* **2004**, *700*, 175-181.
42. Jackson, P.; Parfitt, G. D., Infra-Red Study of the Surface Properties of Rutile. Adsorption of Ethanol, n-Butanol and n-Hexanol. *J. Chem. Soc., Faraday Trans.* **1972**, *68*, 1443-1450.
43. Connor, P. A.; Dobson, K. D.; McQuillan, A. J., Infrared Spectroscopy of the TiO_2/Aqueous Solution Interface. *Langmuir* **1999**, *15*, 2402-2408.
44. Wisnet, A.; Betzler, S. B.; Zucker, R. V.; Dorman, J. A.; Wagatha, P.; Matich, S.; Okunishi, E.; Schmidt-Mende, L.; Scheu, C., Model for Hydrothermal Growth of Rutile Wires and the Associated Development of Defect Structures. *Cryst. Growth Des.* **2014**, *14*, 4658-4663.
45. Hardcastle, T. P.; Brydson, R. M. D.; Livi, K. J. T.; Seabourne, C. R.; Scott, A. J., Ab-Initio Modelling, Polarity and Energetics of Clean Rutile Surfaces in Vacuum and Comparison with Water Environment. *J. Phys.: Conf. Ser.* **2012**, *371*, 012059-012062.
46. Brydson, R.; Sauer, H.; Engel, W.; Thomass, J. M.; Zeitler, E.; Kosugi, N.; Kuroda, H., Electron Energy Loss and X-ray Absorption Spectroscopy of Rutile and Anatase: A Test of Structural Sensitivity. *J. Phys.: Condens. Matter* **1989**, *1*, 797-812.
47. Mitterbauer, C.; Kothleitner, G.; Grogger, W.; Zandbergen, H.; Freitag, B.; Tiemeijer, P.; Hofer, F., Electron Energy-Loss Near-Edge Structures of 3d Transition Metal Oxides Recorded at High-Energy Resolution. *Ultramicroscopy* **2003**, *96*, 469-480.
48. Stoyanov, E.; Langenhorst, F.; Steinle-Neumann, G., The Effect of Valence State and Site Geometry on Ti $L_{3,2}$ and O K Electron Energy-Loss Spectra of Ti_xO_y phases. *Am. Mineral.* **2007**, *92*, 577-586.
49. Cai, J.; Ye, J.; Chen, S.; Zhao, X.; Zhang, D.; Chen, S.; Ma, Y.; Jin, S.; Qi, L., Self-Cleaning, Broadband and Quasi-Omnidirectional Antireflective Structures Based on Mesocrystalline Rutile TiO_2 Nanorod Arrays. *Energy Environ. Sci.* **2012**, *5*, 7575-7581.
50. Jordan, V.; Javornik, U.; Plavec, J.; Podgornik, A.; Recnik, A., Self-Assembly of Multilevel Branched Rutile-Type TiO_2 Structures via Oriented Lateral and Twin Attachment. *Sci. Rep.* **2016**, *6*, 24216-24228.
51. Andersson, S.; Collén, B.; Kruuse, G.; Kuylenstierna, U.; Magnéli, A.; Pestmalis, H.; Åsbrink, S., Identification of Titanium Oxides by X-Ray Powder Patterns. *Acta Chem. Scand.* **1957**, *11*, 1653-1657.
52. Andersson, S.; Collén, B.; Kuylenstierna, U.; Magnéli, A.; Magnéli, A.; Pestmalis, H.; Åsbrink, S., Phase Analysis Studies on the Titanium-Oxygen System. *Acta Chem. Scand.* **1957**, *11*, 1641-1652.
53. Santara, B.; Giri, P. K.; Imakita, K.; Fujii, M., Microscopic Origin of Lattice Contraction and Expansion in Undoped Rutile TiO_2 Nanostructures. *J. Phys. D: Appl. Phys.* **2014**, *47*, 215302-215314.
54. Hanaor, D. A. H.; Sorrell, C. C., Review of the Anatase to Rutile Phase Transformation. *J. Mater. Sci.* **2010**, *46*, 855-874.
55. Pétigny, S.; Mostéfa-Sba, H.; Domenichini, B.; Lesniewska, E.; Steinbrunn, A.; Bourgeois, S., Superficial Defects Induced by Argon and Oxygen Bombardments on (110) TiO_2 Surfaces. *Surf. Sci.* **1998**, *410*, 250-257.
56. Zhou, X.; Liu, N.; Schmuki, P., Ar^+-Ion Bombardment of TiO_2 Nanotubes Creates Co-Catalytic Effect for Photocatalytic Open Circuit Hydrogen Evolution. *Electrochem. Commun.* **2014**, *49*, 60-64.
57. Singh, B. N., Effect of Grain Size on Void Formation During High-Energy Electron Irradiation of Austenitic Stainless Steel. *Philos. Mag.* **1974**, *29*, 25-42.
58. Chen, Y.; Zhang, X.; Wang, J., Radiation Enhanced Absorption of Frank Loops by Nanovoids in Cu. *JOM* **2015**, *68*, 235-241.

59. Lei, Y.; Leng, Y.; Yang, P.; Wan, G.; Huang, N., Theoretical Calculation and Experimental Study of Influence of Oxygen Vacancy on the Electronic Structure and Hemocompatibility of Rutile TiO_2. *Sci. China, Ser. E* **2009**, *52*, 2742-2748.
60. Dow, J. D.; Redfield, D., Toward a Unified Theory of Urbach's Rule and Exponential Absorption Edges. *Phys. Rev. B* **1972**, *5*, 594-610.
61. Perevalov, T. V.; Gritsenko, V. A., Electronic Structure of TiO_2 Rutile with Oxygen Vacancies: Ab Initio Simulations and Comparison with the Experiment. *J. Exp. Theor. Phys.* **2011**, *112*, 310-316.
62. Mattioli, G.; Filippone, F.; Alippi, P.; Amore Bonapasta, A., Ab Initio Study of the Electronic States Induced by Oxygen Vacancies in Rutile and Anatase TiO_2. *Phys. Rev. B* **2008**, *78*, 241201-241204.
63. Mackrodt, W. C.; Simson, E. A.; Harrison, N. M., An Ab Initio Hartree-Fock Study of the Electron-Excess Gap States in Oxygen-Deficient Rutile TiO_2. *Surf. Sci.* **1997**, *384*, 192-200.
64. Pham, H. H.; Wang, L. W., Oxygen Vacancy and Hole Conduction in Amorphous TiO_2. *Phys. Chem. Chem. Phys.* **2015**, *17*, 541-550.

Table of Contents